RSC Advances

PAPER

View Article Online
View Journal | View Issue

Cite this: *RSC Adv.*, 2018, **8**, 32731

Theoretical studies on the structural and spectral properties of two specific C_{54} isomers and the chlorinated species $C_{54}Cl_8$†

Xitong Song, Xiaoqi Li and Jiayuan Qi *

X-ray photoelectron (XPS) and near-edge X-ray absorption fine structure (NEXAFS) spectra as well as the ground-state electronic/geometrical structures of $^{\#540}C_{54}$ captured in experiment and the most controversial isomer $^{\#369}C_{54}$ (C_{2v}- and C_s-symmetry, respectively) have been calculated at the density functional theory (DFT) level. After chlorination, significant changes were observed in the electronic structure and X-ray spectra. Both XPS and NEXAFS spectra showed strong isomer dependence. The results indicated that the "fingerprints" in the X-ray spectra afforded an effective way to identify the fullerene isomers mentioned above. Ultraviolet-visible (UV-Vis) absorption spectroscopy of $C_{54}Cl_8$ was also simulated at the time-dependent (TD) DFT level, and the simulated UV-Vis spectrum was in accordance with the experimental result. The results of this study can provide valuable information for further experimental and theoretical studies of new fullerenes and their derivatives through X-ray and ultraviolet spectroscopy. The study of newly synthesized fullerene isomers and their derivatives using X-ray and UV-Vis spectra offers valuable information for further experimental and theoretical exploration.

Received 2nd August 2018
Accepted 30th August 2018

DOI: 10.1039/c8ra06514d

rsc.li/rsc-advances

1 Introduction

Owing to unique physicochemical properties and the potential in technical applications, fullerenes and their complex compounds have drawn extensive attention from researchers worldwide since the discovery of C_{60} in 1985.[1] Many higher fullerenes such as C_{76}, and C_{78} have been observed and successfully isolated.[2,3] However, for the fullerenes that are smaller than C_{60}, it is ineluctable to have adjacent pentagons, and they violate the isolated pentagon rule (IPR).[4] Due to enhanced local steric strain, non-IPR fullerenes that have contiguous pentagons are unstable and difficult to synthesize and isolate. Fortunately, researchers have made tremendous progress in solving this problem by endohedral modifications (such as encapsulating metal ions or clusters) and exohedral modifications (such as connecting with chlorine or hydrogen), resulting in stable derivatives of the non-IPR cage.[5] Also, many non-IPR fullerenes have been captured such as $^{\#916}C_{56}Cl_{12}$, $^{\#540}C_{54}Cl_8$ and $^{\#271}C_{50}Cl_{10}$ (denominated by Flower's spiral algorithm[6]).[7,8] Due to the large number of isomers and more active chemical properties, the identification of isomers has become a difficult problem for chemists.

As early as 2004, when Xie *et al.* synthesized $C_{50}Cl_{10}$,[8] C_{54} had been captured as a by-product in a chlorine-involving arc-discharge process without isolation. Then, in 2006, Gao *et al.* simulated the relative energy and topological parameters of all 580 isomers of C_{54} using semiempirical PM3 methods, and they predicted the structure of $C_{54}Cl_8$.[9] However, it was not captured for a long time until the breakthrough experiment in 2010. Tan *et al.* successfully captured C_2-$^{\#540}C_{54}Cl_8$ with two pairs of triple sequentially fused pentagons (TSFP) in 2010;[7] they reported detailed characterization by UV-Vis and a series of X-ray crystallography data. The structure of the observed non-IPR isomer was similar to the structure predicted by Gao *et al.*[9] In 2012, Zheng *et al.* probed into the specific selectivity of the chlorination reaction of $C_{54}Cl_8$.[10] The results showed that C_{2v}-$^{\#540}C_{54}$ was the most stable carbon cage, whereas C_2-$^{\#540}C_{54}Cl_8$ was the most stable isomer based on thermodynamics. It is worth mentioning that his group preferred an intriguing theoretical isomer $^{\#369}C_{54}$ and proposed the following question: "why the relative energy of $^{\#369}C_{54}Cl_8$ is lower than that of the captured C_2-$^{\#540}C_{54}Cl_8$?" Herein, we report that $^{\#369}C_{54}$ has 3 pairs of double fused pentagons (DFP) and triple directly fused pentagons (TDFP), and their relative energy is higher than those of $^{\#540}C_{54}$, $^{\#537}C_{54}$ and $^{\#541}C_{54}$ (in order of increasing energy). In the future, $^{\#369}C_{54}Cl_8$ can also be captured in an experiment. Heretofore, some C_{54}-related information ($C_{54}N_6$, $C_{54}H_{24}$, $C_{54}Si_6$, and $B_3N_4C_{54}$) has been reported;[11–14] however, these studies mainly focused on the relative energy and the addition reaction of isomers and did not report in-depth research.

In this report, a series of comparative studies on pure carbon cage and the corresponding chlorinated derivatives of two isomers of C_{54} are presented. We have explored the electronic

College of Chemistry, Fuzhou University, Fuzhou, Fujian, 350116, China. E-mail: jyqi@fzu.edu.cn

† Electronic supplementary information (ESI) available. See DOI: 10.1039/c8ra06514d

structure and optical properties of the two isomers as well as their corresponding chlorinated derivatives by virtue of X-ray and ultraviolet-visible (UV-Vis) spectra. These techniques are atom-specific and sensitive to different local chemical environments of atoms.[15] They have been demonstrated to be effective in the determination of the electronic structure of many molecules, surfaces, or bulk materials. We have simulated the X-ray photoelectron spectra (XPS) and the near-edge X-ray absorption fine structure (NEXAFS) spectra of $^{\#540}C_{54}$ and $^{\#369}C_{54}$ (hereinafter referred to as C_{2v}-$^{\#540}C_{54}$ and C_s-$^{\#369}C_{54}$) as well as their corresponding chlorinated derivatives $^{\#540}C_{54}Cl_8$ and $^{\#369}C_{54}Cl_8$ (hereinafter referred to as C_2-$^{\#540}C_{54}Cl_8$ and C_s-$^{\#369}C_{54}Cl_8$) at the density functional theory (DFT) level. NEXAFS is a sensitive technique for the accurate determination of electronic structure, especially the unoccupied molecular orbitals of molecules; XPS focuses on the information of core orbits, which can thus be used to identify elements and their chemical states in a quantitative manner. In regard to UV-Vis spectroscopy, it is a commonly used technique of characterization in experiments because it can reflect the electronic structure information of the valence band in the system. Many theoretical groups have explored the electronic structures of fullerenes and their corresponding chlorinated derivatives using UV-Vis spectroscopy; the results show that UV-Vis spectra are isomer-dependent, and the identification of electronic structure is credible.[16–20] Hence, we also simulate the UV-Vis spectrum of the experimentally captured isomer C_2-$^{\#540}C_{54}Cl_8$, and the simulation result is in agreement with the experimental results. In general, systematic spectral researches can enhance our comprehension of compounds.

This paper is constituted as follows: Section II describes our computational methods to investigate the electronic structures as well as NEXAFS, XPS and UV-Vis spectra. Section III presents the spectral results and our detailed discussion. Concluding remarks are finally given in Section IV.

2 Computational methods

In this study, we used molecular graphics molecular mechanics, molecular graphics and quantum chemistry to explore the electronic structure and X-ray spectroscopy properties of fullerene in detail. First, the initial coordinates of the two isomers C_s-$^{\#369}C_{54}Cl_8$ and C_2-$^{\#540}C_{54}Cl_8$ were obtained from Zheng *et al.* and the crystallographic data (CIF) of previous experimental results,[7,10] respectively. Subsequently, geometry optimizations of the two C_{54} isomers and the two chlorinated species were achieved at the B3LYP[21,22]/6-31G(d, p) level with the Gaussian 09 quantum chemical package.[23] Considering the dispersive interaction in the functional, we used wB97XD and B3LYP to simulate the optimization of the structure and the energy of the chlorides, respectively. The potential pitfall of the optimization process is that the hybrid density functional method (B3LYP) cannot describe the weak interaction easily. However, according to our calculations, the slight effects on the systems of the present study could be reasonably neglected (please see Table S7 in the ESI†). The obtained geometries were then used to generate X-ray photoelectron spectra (XPS) and near-edge X-ray absorption fine structure spectra (NEXAFS) as well as ultraviolet-visible (UV-Vis) spectra. Ultimately, we chose a much bigger basis set 6-311++G(3df,3pd) to calculate the single point for further energy and charge population analyses. All the energy values we obtained were corrected by ZPE. According to our calculation, the trends of the energy and the stability of corresponding isomers were in agreement with the results of a previous investigation, where the basis set was smaller (such as 3-21G, 6-31G*,6-311G**). Only a slight difference (around 0.1–1 kcal mol^{-1}) could be observed in relative energies. Compared with the results of the previous surveys, we provide more accurate results because of our more rational and authentic computational level.

Also, we use the StoBe program[24] at the DFT level with the gradient corrected Becke (BE88) exchange[25] and the Perdew (PD86) correlation functionals[26] to simulate NEXAFS and XPS spectra. To achieve the convergence of the nuclear hole state, the triple-ζ quality individual gauge for localized orbital (IGLO-III) basis set of Kutzelnigg *et al.* has been chosen for the excited carbon atom, whereas the other non-excited carbon atoms and chlorine atoms have been depicted by model core potentials.[27] We also mention the way that we adopted a full core-hole (FCH) potential method combining a double basis set technique. We used a standard basis set for obtaining the lowest energy of the system, whereas we adopted an auxetic diffuse basis set (19s, 19p, 19d) for simulating NEXAFS spectra in theory.

The FCH method has been validated since NEXAFS can offer precise transition moments and good relative energy in the simulation of fullerene. To obtain the absolute energy, the spectra should be calibrated so that the first spectral feature [1s → the lowest unoccupied molecular orbital (LUMO)] coincides with that from the ΔKohn–Sham (ΔKS) approach.[28,29] Ionization potentials (IPs) have been obtained by a similar calibration using the energy difference between the fully optimized core-ionized state and the ground state. Thus, for all spectra, a shift of +0.2 eV has been employed to account for the differential relativistic effect due to the introduced core hole.[28] Using a Gaussian function with full width at half maximum (FWHM) of 0.3 eV below IP and a Stieltjes imaging approach in the region above,[30,31] NEXAFS spectra can be obtained. The final XPS spectra are generated by broadening the IP values with a Lorentzian line shape with FWHM values set at 0.15 eV and 0.2 eV for different spectral lines.

The UV-Vis absorption spectrum is calculated using time-dependent (TD) DFT calculations at the B3LYP[21,25]/def2-TZVP[32,33] level by the ORCA program.[34] Previous researches indicate that the functionals with varying fractions of the Hartree–Fock (HF) exchange have different excitation energies. To be specific, the excitation energy can increase with increasing HF% such as TPSSh (10% HF), O3LYP (11.61% HF), B3LYP (20% HF) and PBE0 (25% HF).[34,35] During the simulation process, to accelerate the course of calculation, we adopt RIJCOSX approximations combined with the auxiliary basis set def2-TZVP/J. Considering the solvation effect of the toluene solution in the experiment, the solvation energies are estimated at the optimized geometries in the toluene solution using the conductor-like screening model (COSMO).[36] The final UV-Vis

spectrum is obtained by a Gaussian functional convolution with FWHM set at 3000 cm^{-1}, which constitutes an average width for an absorption band observed in the UV-Vis range.[37]

3 Results and discussion

3.1 Geometrical and electronic structure

Optimized structures of the two C_{54} isomers and the two corresponding chlorides are shown in Fig. 1(a) (DFP and TSFP are colored in pink and blue, respectively; the chlorine atoms are colored in green). DFP and TDFP presented in C_s-$^{\#369}C_{54}$ as well as in the corresponding chloride C_s-$^{\#369}C_{54}Cl_8$ are the most distinct geometrical features; besides, both C_{2v}-$^{\#540}C_{54}$ and its corresponding chloride C_2-$^{\#540}C_{54}Cl_8$ show two pairs of TSFP structures. In accordance with the results obtained after optimizing, due to the addition of chlorine atoms, the symmetry of the parent $^{\#540}C_{54}$ is reduced from C_{2v} to C_2, whereas $^{\#369}C_{54}$ still maintains C_s symmetry. The results are consistent with the experimental results and other previous theoretical calculations.

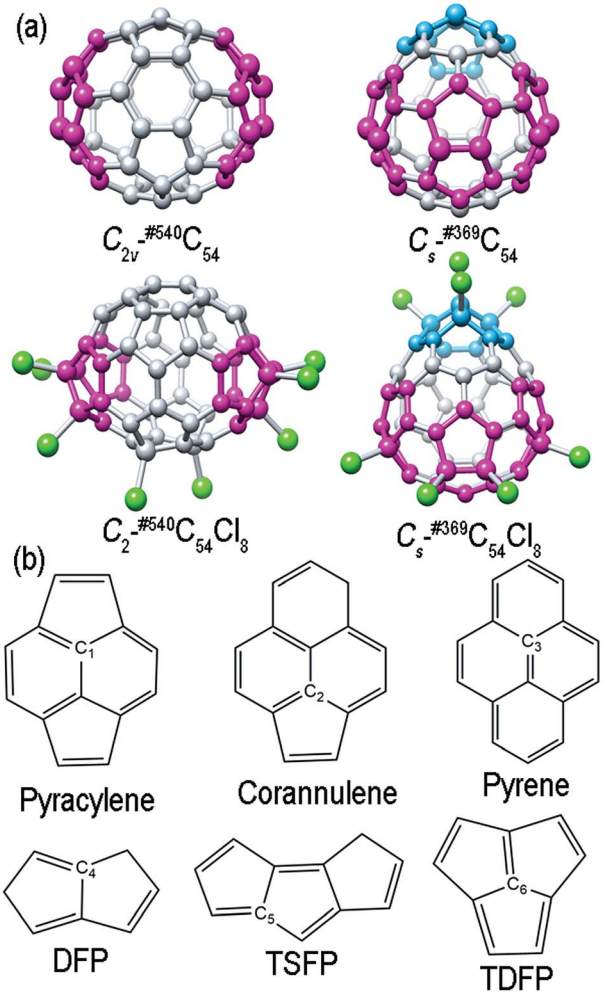

Fig. 1 (a) Optimized structures of the two C_{54} isomers and the corresponding chlorinated species of the selected isomers (TSFP and DFP are colored in pink; TDFP is colored in blue; the chlorine atoms are colored in green). (b) Schematic illustration of the local environment of different types of carbons.

Then, the singlet and triplet states of the two C_{54} isomers and the corresponding chlorides $C_{54}Cl_8$ have been considered (please see Table S5 in the ESI†). Furthermore, the results show that the ground states of the above clusters are all singlet states. Table 1 shows the numerical values of bond lengths, the HOMO (Highest Occupied Molecular Orbital)–LUMO (Lowest Unoccupied Molecular Orbital) gaps of all studied species and the relative total energies of the two fullerene isomers. From the results, we can conclude that although the shortest and the longest bond lengths of the two C_{54} isomers are different, this cannot offer useful information about their relative stabilities as their average values are the same (1.436 Å and 1.436 Å). We have also found that C_s-$^{\#369}C_{54}$ shows higher relative energy [28.76 kcal mol^{-1} at the B3LYP/6-31G(3df, 3pd) level, which is approximately consistent with another calculated result of 30.29 kcal mol^{-1} at the B3LYP/3-21G level]. Meanwhile, the relative energies of the corresponding chlorides show an opposite trend, *i.e.*, the relative energy of C_2-$^{\#540}C_{54}Cl_8$ is higher than that of C_s-$^{\#369}C_{54}Cl_8$ (about 9.57 kcal mol^{-1}), which is in agreement with another calculated result of 9.48 kcal mol^{-1} (at the B3LYP/6-311G** level). The trends of the HOMO–LUMO gap of the parent cages as well as the corresponding chlorides are the same as that of their relative energies. In terms of bond length data, chlorination stretches the C–C bond length of the carbons connected to chlorine atoms. We use X-ray spectroscopy to further study this, as presented in the next section. As displayed in Table 1, we have also calculated the binding energies (BE, indicated as ΔE_b) between the C_{54} backbone and chlorine molecules, which was taken as the chlorine source in the experiment.[7,38] In this study, binding energy is defined as the total energy difference between the chlorinated species and the separated fragments (the carbon cage and n chlorine molecules), *i.e.*,

$$\Delta E_b = E^{\text{chlorinated species}} - (E^{\text{fullerene backbone}} + n \times E^{Cl_2}),$$

where n is 4 for two chlorides. In addition, we have denoted the optimized energy of the chlorinated species as $E^{\text{chlorinated species}}$; for the separated fragments, we have considered the Basis Set Superposition Error (BSSE) and used the energy that is not optimized. The calculations indicate that the chloridization process is favorable in energy as both systems show negative BEs (−576.88 and −601.18 kcal mol^{-1}).

To better understand the interaction between C_{54} and Cl_2 molecules, we have also analyzed the Mulliken charge distribution of C_2-$^{\#540}C_{54}Cl_8$ and C_s-$^{\#369}C_{54}Cl_8$. The sum of Mulliken charges over all carbon atoms (ρ^C) can qualitatively represent the charge transfer during the process of chloridization. As shown in Table 1, the ρ^C values of the two chlorinated species (C_2-$^{\#540}C_{54}Cl_8$ and C_s-$^{\#369}C_{54}Cl_8$) are around 6.859e and 7.587e, respectively, from which we have inferred that the charge of each chlorine atom reaches approximately −1e. The results show strong electron acceptor and donor characteristics of Cl_2 and the C_{54} backbone, respectively. The strong electron transfer and electrostatic interaction uncover great changes in electronic

Table 1 Statistics of bond lengths (Å), HOMO–LUMO gaps (eV) and relative total energies ΔE (kcal mol^{-1}) of the two C_{54} isomers and the corresponding chlorinated species of the selected isomers. Binding energies ΔE_b (kcal mol^{-1}) between the C_{54} backbone and n chlorine molecules as well as the sum of Mulliken charges on all carbon atoms (ρ^C) for the two chlorinated fullerenes ($n = 4$ for both C_2-$^{\#540}C_{54}Cl_8$ and C_s-$^{\#369}C_{54}Cl_8$)

Molecule	Shortest R_{cc}	Longest R_{cc}	Average R_{cc}	Gap	ΔE	ΔE_b	ρ^C
C_{2v}-$^{\#540}C_{54}$	1.374	1.483	1.436	1.271	0.00	—	—
C_s-$^{\#369}C_{54}$	1.387	1.492	1.436	1.630	28.76	—	—
C_2-$^{\#540}C_{54}Cl_8$	1.374	1.612	1.452	3.079	9.57	−576.88	6.859
C_s-$^{\#369}C_{54}Cl_8$	1.369	1.598	1.452	2.311	0.00	−601.18	7.587

and geometrical structures after chlorination. A distinct increase in the C–C bond length indicates structural deformation (Table 1), whereas the changes in the electronic structure are indicated by XPS and NEXAFS spectra, as described below.

Grouping the carbon atoms of fullerenes according to the local environment is a common classification way.[39] As shown in Fig. 1(b), there are three types of carbon sites[40,41] that are commonly distinguished: (1) the pyracylene site C_1, where the carbon atom lying in a pentagon ring is attached to another pentagon by an external bond; (2) the corannulene site C_2, where the carbon atom lying in a pentagon ring is attached to a hexagon by an external bond; (3) the pyrene site C_3, where the carbon atom is a common part of the three hexagons. Besides, there are also new carbon sites in C_s-$^{\#369}C_{54}$ and C_{2v}-$^{\#540}C_{54}$ isomers: (4) the DFP site C_4, where the carbon atom lies in a pentagon–pentagon ring fusion; (5) the TSFP site C_5, where the carbon atom lies in the fused triple sequentially pentagons; (6) the TDFP site C_6, where the carbon atom lies in the intersection of the three fused pentagons. The different combinations of these six carbon sites give rise to different isomers. As an example, there are 28 pyracylene sites, 11 corannulene sites, 5 Pyrene sites and 6 DFP sites for C_s-$^{\#369}C_{54}$ and C_s-$^{\#369}C_{54}Cl_8$; also, there are 38 pyracylene sites, 6 corannulene sites, 2 pyrene sites and 8 TSFP sites for C_{2v}-$^{\#540}C_{54}$ and C_2-$^{\#540}C_{54}Cl_8$.

3.2 XPS

Fig. 2 shows the calculated C1s XPS spectra of different non-equivalent carbon atoms in each C_{54} isomer. As shown in Fig. 2(a), there is a strong peak at around 289.8–290.2 eV for both C_{2v}-$^{\#540}C_{54}$ and C_s-$^{\#369}C_{54}$. Besides, there are three weak peaks at around 289.6 eV, 289.7–289.8 eV (ascribed to TSFP site C_5) and 290.3 eV (ascribed to pyrene site C_3) in the spectrum of C_{2v}-$^{\#540}C_{54}$. By contrast, C_s-$^{\#369}C_{54}$ exhibits four similar peaks mentioned above and also has some different characteristics: two weak peaks appear at around 289.0 eV (ascribed to TDFP site C_6) and 290.6 eV (ascribed to pyrene site C_3). Through the analysis, we have drawn the conclusion that due to the existence of a group of TDFP site carbons, the environment of the carbon atoms changes, which then changes the IP value. Such a character can be used to identify the two different C_{54} isomers. According to previous studies, it is known that even in different fullerenes, the same type of C atom has similar IP values. For instance, the pyracylene and corannulene carbon sites in C_s-$^{\#369}C_{54}$ and C_{2v}-$^{\#540}C_{54}$ show peaks at 289.8–290.2 eV, and the pyrene carbons have higher IP values at 290.2–290.4 eV. In a word, this indicates that the carbon atoms giving rise to the weak peak at lower energies belong to the pentagon–pentagon ring fusion, and the pyrene carbons give rise to the weak peak at higher energies; moreover, the strong peak is associated with the carbon atoms that belong to pyracylene and corannulene carbon sites.

As shown in Fig. 2(b) and 3(c), the XPS spectra of both C_2-$^{\#540}C_{54}Cl_8$ and C_s-$^{\#369}C_{54}Cl_8$ exhibit two groups of peaks: a strong peak at around 289.8–291.2 eV and weak peaks at around 292.2–292.6 eV. It is worth noting that the peak at higher energy is associated with the carbon atoms in the pentagon–pentagon ring fusions, which are connected to the chlorine atoms, whereas the rest of the atoms contribute to the stronger and broader peak. Besides, by comparing the spectra of pure cages and chlorides, it is not difficult to find that chlorination gives rise to a blue shift to a certain degree; especially in TDFP, TSFP and DFP sites directly connect to chlorine atoms. Since the carbon atoms bonded to chlorine atoms have the characteristics of an electron donor, the energy level position of the inner 1s orbital of the chlorinated carbon atoms is reduced, that is, the peaks of C_2-$^{\#540}C_{54}Cl_8$ and C_s-$^{\#369}C_{54}Cl_8$ appear in the high-energy regions of the XPS spectra. This result coincides with previously reported results on halogenation of carbon compounds, which indicates that the binding energy of carbon 1s electrons can increase differently depending on the bond type of the carbon atoms.[42,43] The calculated result again indicates the effective change in geometrical and electronic structures of the C_{54} backbone after chlorination.

Hence, XPS spectra can be regarded as an effective tool to identify isomers with different symmetries in principle.

3.3 NEXAFS

The calculated NEXAFS spectra of the two C_{54} isomers as well as the contributions from various types of carbons are displayed in Fig. 3. The total NEXAFS spectrum in this section is based on different relative abundances of different types of carbons. As shown in Fig. 3(a), both C_{2v}-$^{\#540}C_{54}$ and C_s-$^{\#369}C_{54}$ exhibit eight major peaks, which are labeled as A–H (marked in the ascending order of energy). In Fig. 3(a), we can see that the NEXAFS spectra of the two isomers show a distinct difference by the peaks in the range between 283 and 287 eV. To be specific, compared to C_s-$^{\#369}C_{54}$, which exhibits two distinct sharp peaks (marked as C and D), C_{2v}-$^{\#540}C_{54}$ shows a stronger peak C and

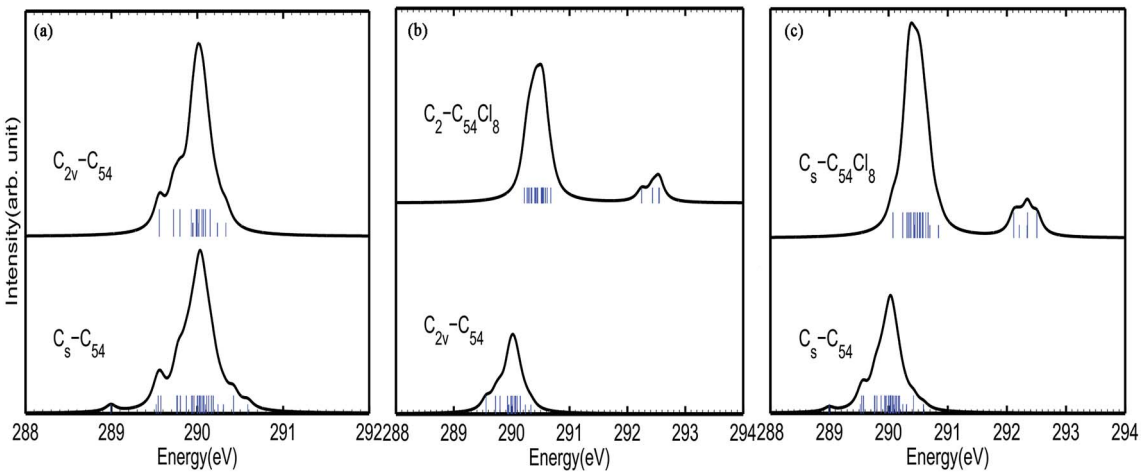

Fig. 2 Calculated 1s ionization potentials (IPs, denoted as bars) of different symmetry-independent carbon atoms in (a) each C_{54} isomer (b) C_{2v}-C_{54} and its corresponding chlorinated species and (c) C_s–C_{54} and its corresponding chlorinated species; the XPS spectra are generated from these IPs through a Lorentzian convolution with FWHM = 0.1 eV, 0.2 eV and 0.2 eV, respectively.

a wider peak D, and it has a right shoulder peak labeled as E. Slight differences can also be observed in high-energy areas; especially, C_s-$^{\#369}C_{54}$ exhibits a weak peak H around 289 eV, which is almost non-existent in C_{2v}-$^{\#540}C_{54}$.

Fig. 3(b) and (c) show the contributions of different carbon types to C_{2v}-$^{\#540}C_{54}$ and C_s-$^{\#369}C_{54}$, respectively. In Fig. 3(b), we can see that peak A arises from TSFP, which is peculiar to C_{2v}-$^{\#540}C_{54}$; this can be viewed as "fingerprints". The pyracylene, corannulene and TSFP site carbons all make important contributions to peak B, and the pyrene site carbon leads to peak G. As for peaks C, D, E, F and H, they significantly originate from all types of carbons. In Fig. 3(c), we can see that peak A arises from TDFP and DFP, which are peculiar to C_s-$^{\#369}C_{54}$; this can be regarded as "fingerprints". Besides, pyracylene, corannulene and pyrene site carbons mainly contribute to peak B. The remaining peaks arise from all five types of carbons.

In the same way, we have calculated the total NEXAFS spectra of C_{2v}-$^{\#540}C_{54}Cl_8$ and C_s-$^{\#369}C_{54}Cl_8$ as well as the contributions from the four types of carbons, as displayed in Fig. 4 and Fig. 5, respectively. From Fig. 4(a) and 5(a), we can observe that the NEXAFS spectra of chlorine derivatives have strong peaks in both high-energy region (290–292 eV) and low-energy region (284–287 eV). Clearly, the peaks in the high-energy region do not exist in the parent cages. Therefore, peaks E and F for C_{2v}-$^{\#540}C_{54}Cl_8$ as well as peaks F, G and H for C_s-$^{\#369}C_{54}Cl_8$ can be regarded as "fingerprints" to identify the two chlorine derivatives with different symmetries. Furthermore, as shown in Fig. 4(b), TSFP and corannulene carbon sites contribute to "fingerprints"; TDFP and DFP carbon sites contribute to "fingerprints", as shown in Fig. 5(b). All these carbon sites (TSFP, TDFP and DFP) are novel types of carbon atoms present in the newly captured C_{54} chlorides. By a careful consideration of Fig. 3, 4 and 5, we can find that all types of C atoms show varying degrees of blueshifts after chlorination. Specifically, distinct blue shifts of about 2 eV and 3 eV have been observed in TSFP, TDFP and DFP carbon sites. In addition, the other carbon atoms show a small blue shift of about 0.2 eV. Furthermore, the peaks of TSFP, TDFP and DFP carbon sites are stronger after

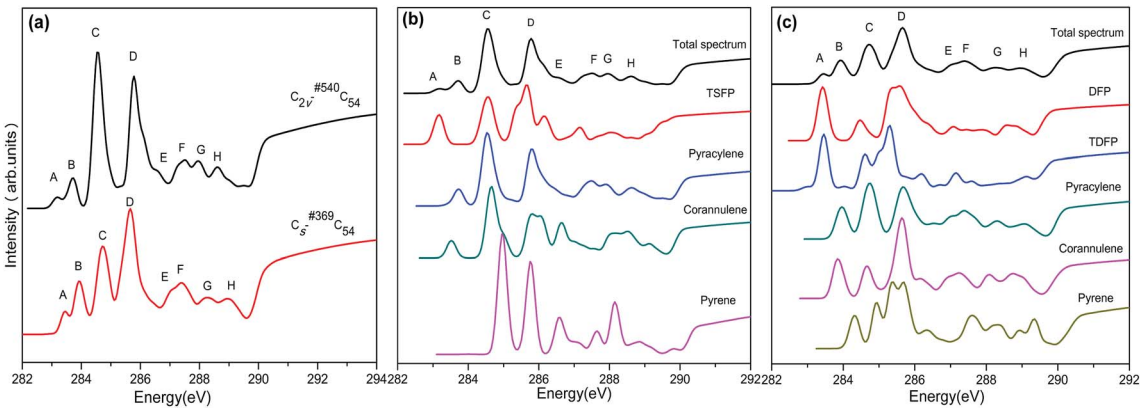

Fig. 3 Calculated (a) total NEXAFS spectra of the two C_{54} isomers as well as type-specific contributions for (b) C_{2v}-C_{54} and (c) C_s–C_{54}. Each total spectrum is obtained by the weighted (according to their relative abundance) summation of all type-specific spectra.

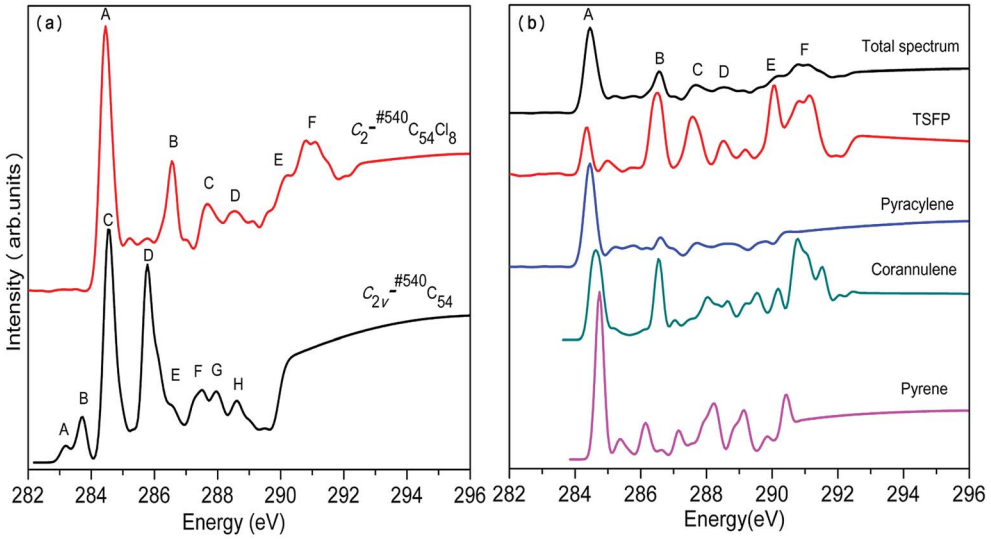

Fig. 4 Calculated (a) total NEXAFS spectra of C_{2v}-#540C_{54} and its corresponding chlorinated species as well as type-specific contributions for (b) C_2-#540$C_{54}Cl_8$. Each total spectrum is obtained by the weighted (according to their relative abundance) summation of all type-specific spectra.

chlorination. In a word, all these differences clarify that chlorination effectively changes the electronic structure of the main chain of C_{54}.

In conclusion, we observed clear differences between the two C_{54} isomers and their corresponding chlorine derivatives from NEXAFS spectra due to the difference between the isomers as well as the effects of chlorination on the geometry and the electronic structure of fullerene. Thus, peaks E and F for C_{2v}-#540$C_{54}Cl_8$ as well as peaks F, G and H for C_s-#369$C_{54}Cl_8$ could reasonably be viewed as "fingerprints" to identify the two isomers. Then, simulation results confirmed that the NEXAFS spectrum could provide effective identification information for non-IPR fullerenes.

3.4 UV-Vis absorption spectrum

In addition to the NEXAFS and XPS spectra mentioned above for the different isomers of C_{54} fullerene and the corresponding chlorides, we have also simulated the UV-Vis absorption spectrum of C_{2v}-#540$C_{54}Cl_8$ on the TD-DFT level. Considering the effect of the proportion of the Hartree–Fock (HF) exchange on results, we have managed to simulate the spectrum by using functionals with different HF%. In conclusion, we found that the generated spectrum using the functional with B3LYP (20% HF), shown in Fig. 6, is consistent with the experimental result. The vertical coordinates of the UV-Vis absorption spectrum obtained by simulation are convolved by a Gaussian function with FWHM = 3000 cm^{-1}. As displayed in Fig. 6, the absorption

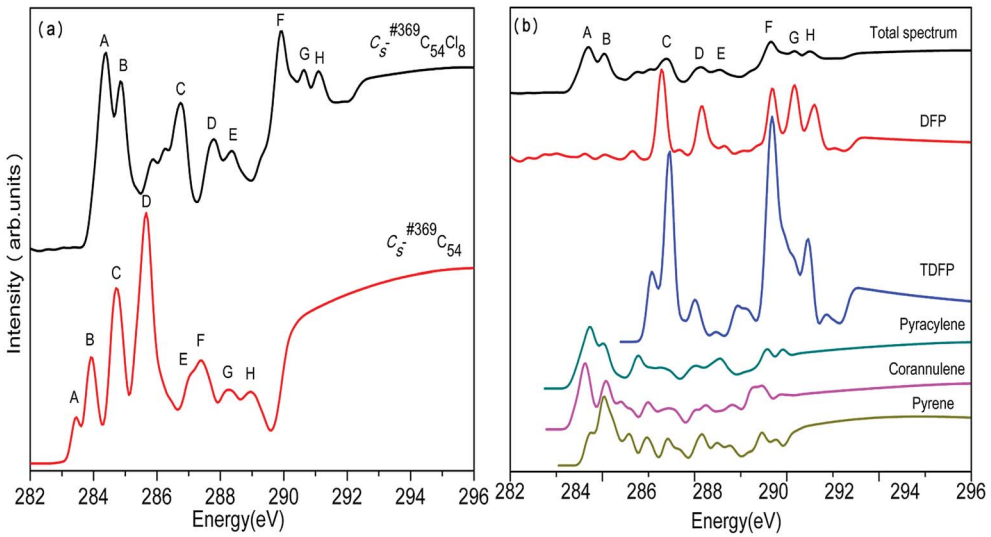

Fig. 5 Calculated (a) total NEXAFS spectra of C_s-#369C_{54} and its corresponding chlorinated species as well as type-specific contributions for (b) C_s-#369$C_{54}Cl_8$. Each total spectrum is obtained by the weighted (according to their relative abundance) summation of all type-specific spectra.

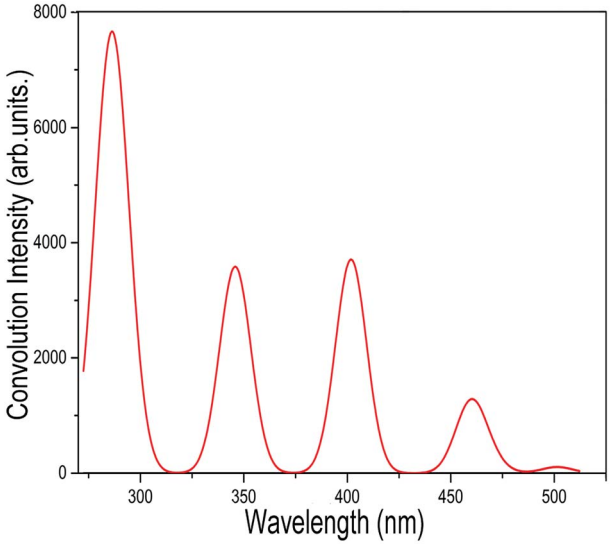

Fig. 6 Calculated UV-Vis spectrum of C_2-$^{\#540}C_{54}Cl_8$, which is generated by a Gaussian functional convolution with FWHM = 3000 cm^{-1}.

spectrum has five different feature peaks, of which four absorption peaks have larger convolutional intensities at about 288, 341, 465 nm and an exceedingly weak crest at about 504 nm.

We have also listed the TD-DFT calculated adsorption wavelength, excitation energies, oscillator strengths (f_{osc}) and the leading transition composition for further explanation. Table 2 lists the excitations with f_{osc} > 0.001 as well as the contributions of more than 10% in the transition processes. In accordance with our calculations, each strong peak observed in the spectrum is not derived from one excitation energy only. For instance, the empirical strong peak at 288 nm stems from the cooperative contributions of the electronic excitations with the energies at 283.3, 285.5, 289 and 289.4 nm. The absorption peak at 341 nm mainly corresponds to the excitation HOMO → LUMO+5(72.6%), HOMO−5 → LUMO+2 (41.0%), HOMO−3 → LUMO+4 (29.2%) and HOMO → LUMO+5 (11.2%). Besides, compared with the other strong peaks, there is a weak peak at 504 nm. The other peaks of the absorption spectrum in Fig. 6 are detailed in Table 2. Previous studies have shown that the TD-DFT method slightly overestimates the excitation energy and produces a certain deviation; thus, it is reasonable to hold the view that the UV-Vis absorption spectrum obtained by our simulation is consistent with the experimental results. This method should be considered as a conducive means for characterizing the electronic structures of fullerenes and their derivatives. Simultaneously, it will be a significant application to provide rational and appropriate theoretical explanations for experimental phenomena. Other relevant details are shown in the ESI.†

4 Conclusion

We have calculated the electronic structures and the XPS and NEXAFS spectra of the two C_{54} isomers C_{2v}-$^{\#540}C_{54}$ and C_s-$^{\#369}C_{54}$ as well as their corresponding chlorides C_2-$^{\#540}C_{54}Cl_8$ and C_s-$^{\#369}C_{54}Cl_8$ at the DFT level. The UV-Vis absorption spectra of the chloride C_2-$^{\#540}C_{54}Cl_8$ are also obtained by the TD-DFT method. Both XPS and NEXAFS spectra show that the chlorination process has a significant effect on the carbon cage, and they also demonstrate strong isomer dependence. In particular, the carbon atoms at the fusions of the pentagon–pentagon rings (DFP, TDFP and TSFP) show specific signals that are characteristic of C_{2v}-$^{\#540}C_{54}$ and C_s-$^{\#369}C_{54}$ as well as C_2-$^{\#540}C_{54}Cl_8$ and C_s-$^{\#369}C_{54}Cl_8$. In NEXAFS and XPS spectra, the C atoms at the fusions of pentagon–pentagon rings (DFP, TDFP and TSFP) contribute to the fingerprint peaks of non-IPR fullerenes and the corresponding chlorinated derivatives,

Table 2 TD-DFT-calculated wavelength λ (nm), excitation energies E (eV), oscillator strengths f_{osc} (a.u.), leading transition compositions (H and L refer to HOMO and LUMO, respectively) and the comparison with experimental values for optically allowed singlet excitation states of C_2-$^{\#540}C_{54}Cl_8$

Exp. λ[a]	State	Calc. λ	Calc. E	f_{osc}[b]	Leading transition configurations[c] (%)
	S_{66}	283.3	4.376	0.01970	H−5 → L+6(57.0), H−10 → L+1(12.7)
	S_{65}	285.5	4.342	0.00719	H−3 → L+8(55.0), H−2 → L+8(10.3), H−8 → L+2(10.2)
	S_{62}	289	4.290	0.00588	H−12 → L(48.3)
	S_{61}	289.4	4.284	0.00595	H−10 → L+1(54.0), H−9 → L+1(10.7)
288	S_{64}	289.4	4.284	0.00464	H−13 → L(25.22), H−15 → L(24.9), H−12 → L+1(17.0)
341	S_{29}	344.9	3.595	0.03093	H → L+5(72.6)
	S_{28}	346.9	3.574	0.01065	H−5 → L+2(41.0), H−3 → L+4(29.2), H → L+5(11.2)
406	S_{13}	401.7	3.087	0.09950	H−4 → L(46.7), H → L+3(24.7)
465	S_5	460.1	2.695	0.04826	H−3 → L+1(34.4), H−2 → L+1(32.9), H−1 → L+1(25.6)
	S_4	470.3	2.637	0.00938	H−2 → L(38.5), H−1 → L(36.8), H−3 → L(17.8)
504	S_1	501.2	2.474	0.00586	H → L+1(94.7)

[a] Experimental values from ref. 6. [b] Only the excitations with f_{osc} > 0.001 are listed. [c] Contributions of less than 10% are omitted.

which appear in the lower and higher energy regions, respectively. In other words, there is a large blue shift in the NEXAFS and XPS spectra after chlorination. In addition, the calculated UV-Vis absorption spectra are greatly consistent with previous experimental results. Therefore, the results indicate that X-ray and UV-Vis spectroscopy can afford useful methods for further experimental and theoretical studies of fullerene isomers and their derivatives.

Conflicts of interest

There are no conflicts to declare.

Acknowledgements

This work was supported by the National Natural Science Foundation of China (Grant No. 21503042), the Research Fund for the Doctoral Program of Higher Education of China (20123514120003), Natural Science Foundation of Fujian Province (2014J05015), Foundation of Educational Commission of Fujian Province (JA14036) and Fuzhou University (2012-XQ-12).

References

1 H. W. Kroto, J. R. Heath, S. C. O'Brien, R. F. Curl and R. E. Smalley, *Nature*, 1985, **318**, 162–163.
2 R. Ettl, I. Chao, F. Diederich and R. L. Whetten, *Nature*, 1991, **353**, 149–153.
3 F. Diederich, R. L. Whetten, C. Thilgen, R. Ettl, I. Chao and M. M. Alvarez, *Science*, 1991, **254**, 1768–1770.
4 H. Kroto, *Nature*, 1987, **329**, 529–531.
5 Y.-Z. Tan, S.-Y. Xie, R.-B. Huang and L.-S. Zheng, *Nat. Chem.*, 2009, **1**, 450–460.
6 P. W. Fowler and D. E. Manolopoulos, *An atlas of fullerenes*, Oxford Univ. Press, Oxford, 1995.
7 Y. Z. Tan, J. Li, F. Zhu, X. Han, W. S. Jiang, R. B. Huang, Z. P. Zheng, Z. Z. Qian, R. T. Chen, Z. J. Liao, S. Y. Xie, X. Lu and L. S. Zheng, *Nat. Chem.*, 2010, **2**, 269–273.
8 S.-Y. Xie, F. Gao, X. Lu, R.-B. Huang, C.-R. Wang, X. Zhang, M.-L. Liu, S.-L. Deng and L.-S. Zheng, *Science*, 2004, **304**, 699.
9 X. Gao and Y. Zhao, *J. Comput. Chem.*, 2007, **28**, 795–801.
10 H. Zheng, J. Li and X. Zhao, *Dalton Trans.*, 2012, **41**, 14281–14287.
11 M. Bühl, *Chem. Phys. Lett.*, 1995, **242**, 580–584.
12 G. Mehta and P. S. Sarma, *Tetrahedron Lett.*, 2002, **43**, 6557–6560.
13 Y. Yong, S. Lv, R. Zhang, Q. Zhou, X. Su, T. Li and H. Cui, *RSC Adv.*, 2016, **6**, 89080–89088.
14 A. K. Srivastava, S. K. Pandey and N. Misra, *J. Nanostruct. Chem.*, 2016, **6**, 103–109.
15 J. Stöhr, *NEXAFS spectroscopy*, Springer-Verlag, Berlin, 1992.
16 J. Qi, W. Hua and B. Gao, *Chem. Phys. Lett.*, 2012, **539**, 222–228.
17 J. Qi, X. Hu, H. Zhu and M. Zheng, *Phys. Chem. Chem. Phys.*, 2016, **18**, 8049–8058.
18 J. Qi, H. Zhu, M. Zheng and X. Hu, *RSC Adv.*, 2016, **6**, 96752–96761.
19 N. Chen, C. M. Beavers, M. Mulet-Gas, A. Rodríguez-Fortea, E. J. Munoz, Y.-Y. Li, M. M. Olmstead, A. L. Balch, J. M. Poblet and L. Echegoyen, *J. Am. Chem. Soc.*, 2012, **134**, 7851–7860.
20 B. Brena and Y. Luo, *J. Chem. Phys.*, 2003, **119**, 7139–7144.
21 C. Lee, W. Yang and R. G. Parr, *Phys. Rev. B: Condens. Matter Mater. Phys.*, 1988, **37**, 785.
22 A. D. Becke, *J. Chem. Phys.*, 1993, **98**, 5648–5652.
23 M. J. Frisch, G. W. Trucks, H. B. Schlegel, G. E. Scuseria, M. A. Robb, J. R. Cheeseman, G. Scalmani,V. Barone, B. Mennucci, G. A. Petersson, H. Nakatsuji, M. Caricato, X. Li, H. P. Hratchian, A. F. Izmaylov, J. Bloino, G. Zheng, J. L. Sonnenberg, M. Hada, M. Ehara, K. Toyota, R. Fukuda, J. Hasegawa, M. Ishida, T. Nakajima, Y. Honda, O. Kitao, H. Nakai, T. Vreven, J. A. Montgomery Jr, J. E. Peralta, F. Ogliaro, M. J. Bearpark, J. Heyd, E. N. Brothers, K. N. Kudin, V. N. Staroverov, R. Kobayashi, J. Normand, K. Raghavachari, A. P. Rendell, J. C. Burant, S. S. Iyengar, J. Tomasi, M. Cossi, N. Rega, N. J. Millam, M. Klene, J. E. Knox, J. B. Cross, V. Bakken, C. Adamo, J. Jaramillo, R. Gomperts, R. E. Stratmann, O. Yazyev, A. J. Austin, R. Cammi, C. Pomelli, J. W. Ochterski, R. L. Martin, K. Morokuma, V. G. Zakrzewski, G. A. Voth, P. Salvador, J. J. Dannenberg, S. Dapprich, A. D. Daniels, Ö. Farkas, J. B. Foresman, J. V. Ortiz, J. Cioslowski and D. J. Fox, *GAUSSIAN 09 (Revision D.01)*, Gaussian Inc., Wallingford, CT, 2009.
24 K. Hermann, L. Pettersson, M. Casida, C. Daul, A. Goursot, A. Koester, E. Proynov, A. St-Amant, D. Salahub and V. Carravetta, StoBe-deMon (Version 3.0) and Documentation for STOBE2007, *StoBe Software*, Stockholm, 2007.
25 A. D. Becke, *Phys. Rev. A*, 1988, **38**, 3098.
26 J. P. Perdew, *Phys. Rev. B: Condens. Matter Mater. Phys.*, 1986, **33**, 8822.
27 W. Kutzelnigg, U. Fleischer and M. Schindler, *NMR-basic principles and progress*, Springer, Verlag, Heidelberg, 1990.
28 L. Triguero, O. Plashkevych, L. G. M. Pettersson and H. Ågren, *J. Electron Spectrosc. Relat. Phenom.*, 1999, **104**, 195–207.
29 C. Kolczewski, R. Püttner, O. Plashkevych, H. Ågren, V. Staemmler, M. Martins, G. Snell, A. S. Schlachter, M. Sant'Anna, G. Kaindl and L. G. M. Pettersson, *J. Chem. Phys.*, 2001, **115**, 6426–6437.
30 P. W. Langhoff, *Electron-molecule and photon-molecule collisions*, Springer, New York, 1979.
31 P. W. Langhoff, *Theory and application of moment methods in many-fermion systems*, Springer, New York, 1980.
32 A. Schäfer, H. Horn and R. Ahlrichs, *J. Chem. Phys.*, 1992, **97**, 2571–2577.
33 F. Weigend and R. Ahlrichs, *Phys. Chem. Chem. Phys.*, 2005, **7**, 3297–3305.
34 F. Neese, *Wiley Interdiscip. Rev.: Comput. Mol. Sci.*, 2012, **2**, 73–78.
35 R. J. Magyar and S. Tretiak, *J. Chem. Theory Comput.*, 2007, **3**, 976.

36 A. Klamt and G. Schüürmann, *J. Chem. Soc., Perkin Trans. 2*, 1993, 799–805.
37 S.-W. Tang, J.-D. Feng, Y.-Q. Qiu, H. Sun, F.-D. Wang, Z.-M. Su, Y.-F. Chang and R.-S. Wang, *J. Comput. Chem.*, 2010, **32**, 658–667.
38 C. L. Gao, X. Li, Y. Z. Tan, X. Z. Wu, Q. Zhang, S. Y. Xie and R. B. Huang, *Angew. Chem., Int. Ed.*, 2014, **53**, 7853–7855.
39 A. Bassan, M. Nyberg and Y. Luo, *Phys. Rev. B: Condens. Matter Mater. Phys.*, 2002, **65**, 165402.
40 F. Diederich and R. L. Whetten, *Acc. Chem. Res.*, 1992, **25**, 119–126.
41 T. Heine, G. Seifert, P. Fowler and F. Zerbetto, *J. Phys. Chem. A*, 1999, **103**, 8738–8746.
42 E. Papirer, R. Lacroix, J.-B. Donnet, G. Nanse and P. Fioux, *Carbon*, 1994, **32**, 1341–1358.
43 E. Papirer, R. Lacroix, J.-B. Donnet, G. Nansé and P. Fioux, *Carbon*, 1995, **33**, 63–72.